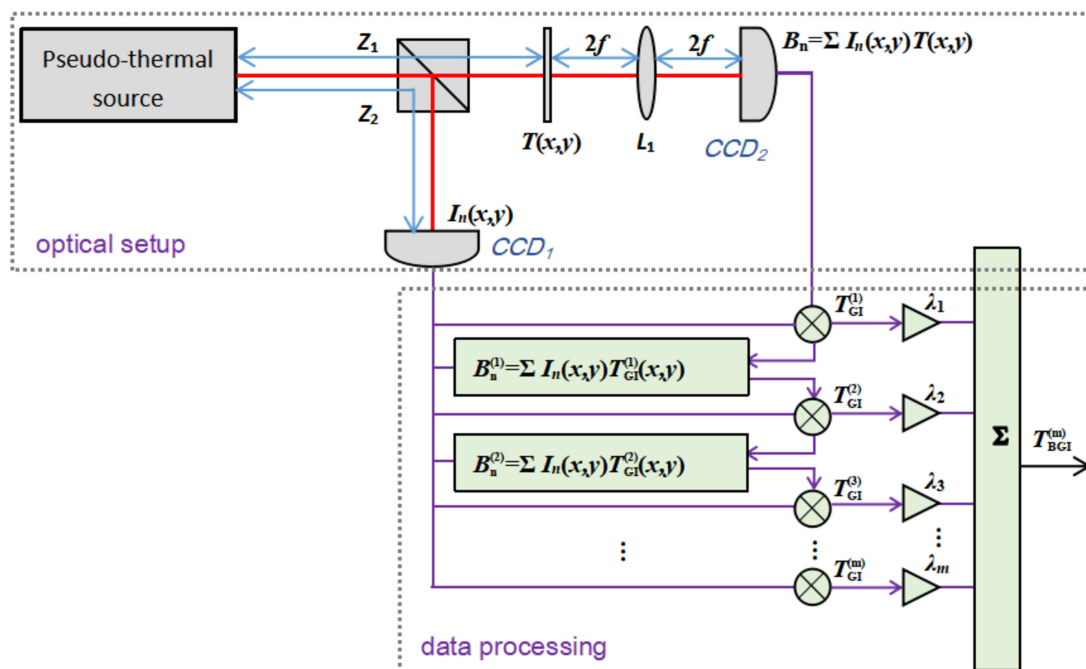


# Object Reconstruction Using the Binomial Theorem for Ghost Imaging

Volume 10, Number 6, December 2018

Cong Yue  
Ping Chen  
Xiaofeng Lv  
Chenglong Wang  
Shuxu Guo  
Junfeng Song  
Wenlin Gong  
Fengli Gao



# Object Reconstruction Using the Binomial Theorem for Ghost Imaging

Cong Yue,<sup>1</sup> Ping Chen,<sup>1</sup> Xiaofeng Lv<sup>ID</sup>,<sup>1</sup> Chenglong Wang<sup>ID</sup>,<sup>2</sup>  
Shuxu Guo,<sup>1</sup> Junfeng Song,<sup>1</sup> Wenlin Gong,<sup>2</sup> and Fengli Gao<sup>ID</sup><sup>1</sup>

<sup>1</sup>State Key Laboratory on Integrated Optoelectronics, College of Electronic Science and Engineering, Jilin University, Changchun 130012, China

<sup>2</sup>Key Laboratory for Quantum Optics and Center for Cold Atom Physics of CAS, Shanghai Institute of Optics and Fine Mechanics, Chinese Academy of Sciences, Shanghai 201800, China

DOI:10.1109/JPHOT.2018.2880430

1943-0655 © 2018 IEEE. Translations and content mining are permitted for academic research only. Personal use is also permitted, but republication/redistribution requires IEEE permission.

See [http://www.ieee.org/publications\\_standards/publications/rights/index.html](http://www.ieee.org/publications_standards/publications/rights/index.html) for more information.

Manuscript received October 17, 2018; accepted November 6, 2018. Date of publication November 9, 2018; date of current version November 22, 2018. This work was supported in part by the National Key Research and Development Program of China under Grant 2016YFE0200700, in part by the National Natural Science Foundation of China under Grants 61627820 and 61571427, in part by the Natural Science Foundation of the Science and Technology Development Program of the Jilin Province, China under Grant 20160101284JC, in part by the Youth Innovation Promotion Association of the Chinese Academy of Sciences, and in part by the Open Foundation of State Key Laboratory of Luminescence and Applications, China under Grant SKLA-2016-05. Corresponding authors: Wenlin Gong and Fengli Gao (e-mail: gongwl@siom.ac.cn; gaofl@jlu.edu.cn).

**Abstract:** Noise term in the reconstruction matrix in ghost imaging is a major cause of blurring imaging results. To remedy this problem, we propose a new ghost imaging method based on the binomial theorem to reduce the level of noise. In our method, images with low-level noise can be generated by constructing a binomial formula using high-order imaging results that are acquired by reintroducing the reconstruction result back into the imaging formula repeatedly. Experimental and simulation results demonstrate that our method is effective in improving imaging quality and the anti-interference performance and reducing computing time, making it useful for practical applications.

**Index Terms:** Imaging processing, coherence imaging, photon statistics, quantum optics.

## 1. Introduction

Ghost imaging (GI), which is different from traditional imaging technology, uses the second-order or high-order correlation function of the light field to realize the separation of the detection and imaging, so as to achieve nonlocal imaging [1]–[14]. Therefore, it is very useful for imaging in noisy or harsh environments. GI was originally implemented using entangled photon pairs with quantum illumination, and it can also be completely explained as a classical phenomenon [1], [2], [12]–[14]. Subsequently, pseudo-thermal light, thermal light, and other light sources have also been proven to be effective [5], [7], [12]–[18], thereby reducing the light source requirement and facilitating practical application of the technique; even microwaves and X-rays have been proven to be feasible by experiments [19], [20]. In addition, studies have demonstrated that imaging through a variety of optical media is also possible [21]–[23]. Subsequently, various practical applications have also been further studied [22], [24]–[26]. However, traditional GI technology has poor imaging quality and requires a large number of measurements, which greatly limits its application.

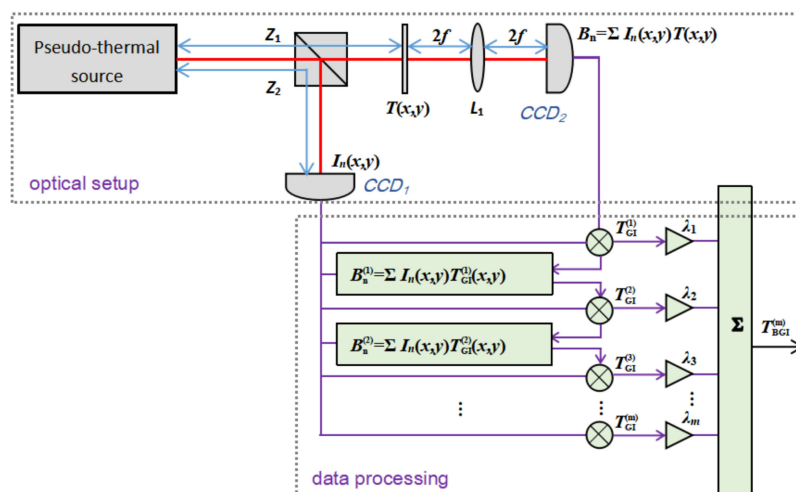


Fig. 1. Schematic of the BGI system.  $Z_1$  is the distance of the object path and  $Z_2$  is the distance of the reference path;  $f$  is the focal length of the lens and  $L_1$  is the transmission aperture of the lens.

Therefore, numerous improved reconstruction algorithms have been proposed to address the problem of traditional GI [27]–[41]. Differential ghost imaging (DGI) and normalized ghost imaging (NGI) are proposed by modifying the imaging formula to improve the quality of imaging and reduce the effects of noise on the imaging process [28], [31]. Compressive-sensing ghost imaging (CSGI) can greatly enhance visibility under a small number of measurements far below the Nyquist limit, but the complexity of CSGI will lead to a longer computing time and consume considerable memory resources [27], [30]. Iterative denoising of ghost imaging (IDGI) and iterative ghost imaging (IGI) combine the iterative process to give an accurate estimate of the actual noise affecting image quality. Better imaging results can be achieved by adjusting some parameters, and these can be obtained by conducting experiments [32], [33]. According to matrix analysis, pseudo-inverse ghost imaging (PGI) and scalar-matrix-structured ghost imaging (SMGI) have been proposed, and the new matrix can be applied to improve imaging quality significantly [34], [35], [37], [38]. However, PGI has a relatively poor robust performance, and SMGI takes more time.

In this paper, we propose a novel method based on the binomial theorem, referred to as “binomial-theorem ghost imaging” (BGI), based on GI and “binomial-theorem differential ghost imaging” (BDGI) based on DGI to eliminate noise in the imaging process. Unlike previous algorithms based on matrices such as CSGI, PGI, and SMGI, these methods construct all observation points as a matrix and directly modify or solve this characteristic matrix. We extract the information from the matrix by repeating the reconstruction process to reduce imaging noise. Through analysis of the matrix in the reconstruction process, a high-order noise term with lower noise values can be obtained by returning the imaging results back to the equation. The level of the noise can be reduced by using the binomial theorem. Experiments show that both DGI and GI can be effectively denoised by our method, and it achieves satisfactory imaging results with a small amount of time and low memory consumption. Our algorithm eliminates the construction of immense matrices, so the demand for hardware resources is also low.

## 2. Experimental Setup and Imaging Principle

A schematic of the experimental setup is shown in Fig. 1. The system can be divided into an optical part and a processing part. The pseudo-thermal light source creates a constantly changing speckle field, which is produced by passing a laser beam (with a wavelength of 650 nm) through a slowly rotating ground glass, and the light is then divided by a 50:50 beam splitter into two paths: the

object path, containing information of the object, and the reference path, carrying information of the original beam. The object path is modulated by the object with a transmission coefficient  $T(x, y)$  and then measured by a bucket detector without spatial resolution (or a charge-coupled device (CCD) summing the intensity of all pixel points), and the  $n$ th measurement is recorded as  $B_n$ . The reference beam, after propagating the same distance in free space, is directly collected by a CCD with spatial resolution and the  $n$ th measurement is recorded as  $I_n(x, y)$ . In conventional GI, the object's image  $T_{GI}(x, y)$  can be reconstructed by computing the second-order correlation function between  $B_n$  and  $I_n(x, y)$ :

$$T_{GI}(x, y) = \frac{1}{N} \sum_{n=1}^N (B_n - \langle B \rangle) (I_n(x, y) - \langle I_N(x, y) \rangle) \quad (1)$$

where  $\langle B \rangle = \frac{1}{N} \sum_{n=1}^N B_n$  and  $\langle I_N(x, y) \rangle = \frac{1}{N} \sum_{n=1}^N I_n(x, y)$  represent the ensemble averages of  $B_n$  and  $I_n(x, y)$ , respectively.

As can be seen, Eq. (1) is the summation of multiple measurements. Consequently, by constructing the observation matrix, the algebraic formula can be transformed into matrix form. Provided that the object and each measurement of reference beam data are  $p \times q$  pixels, then after  $N$  measurements we can construct an  $N \times K$  ( $K = p \times q$ ) observation matrix  $\Phi$  given by [34]

$$\Phi = \begin{bmatrix} I_1(1, 1) & I_1(1, 2) & I_1(1, 3) & \cdots & I_1(1, q) & I_1(2, 1) & I_1(2, 2) & \cdots & I_1(p, q) \\ I_2(1, 1) & I_2(1, 2) & I_2(1, 3) & \cdots & & & & \cdots & I_2(p, q) \\ \vdots & & & & & & & \ddots & \vdots \\ I_N(1, 1) & I_N(1, 2) & I_N(1, 3) & \cdots & & & & \cdots & I_N(p, q) \end{bmatrix} \quad (2)$$

Then, the imaging formula can be written as

$$\begin{aligned} \mathbf{T}_{GI}(x, y) &= \frac{1}{N} (\Phi - \mathbf{I} \langle \Phi \rangle)^T (\mathbf{B} - \mathbf{I} \langle B \rangle) \\ &= \frac{1}{N} (\Phi - \mathbf{I} \langle \Phi \rangle)^T (\Phi - \mathbf{I} \langle \Phi \rangle) \mathbf{T} \\ &= \frac{1}{N} \Psi^T \Psi \mathbf{T} \end{aligned} \quad (3)$$

where  $\langle \Phi \rangle = [\langle I_N(1, 1) \rangle \langle I_N(1, 2) \rangle \cdots \langle I_N(p, q) \rangle]$  represents a  $1 \times K$  row vector, which indicates the average intensity distribution of the reference beam, and  $\mathbf{I} = [1 \ 1 \ \cdots \ 1]^T$  denotes an  $N \times 1$  column vector whose elements are all 1. Similarly,  $\mathbf{B} = [B_1 \ B_2 \ \cdots \ B_N]^T$  denotes an  $N \times 1$  column vector that represents the information of the object path. Finally,  $\mathbf{T} = [T(1, 1) \ T(1, 2) \ \cdots \ T(p, q)]^T$  is a  $K \times 1$  column vector representing the object's transmission coefficient  $T(x, y)$ .

Likewise, DGI can be expressed in the form of a matrix as follows [35], [39]:

$$\begin{aligned} \mathbf{T}_{DGI}(x, y) &= \frac{1}{N} (\Phi - \mathbf{I} \langle \Phi \rangle)^T \left( \mathbf{B} - \frac{\langle B \rangle}{\langle R \rangle} \mathbf{R} \right) \\ &= \frac{1}{N} (\Phi - \mathbf{I} \langle \Phi \rangle)^T (\Phi - \mathbf{I} \langle \Phi \rangle) \Delta \mathbf{T} \\ &= \frac{1}{N} \Psi^T \Psi \Delta \mathbf{T} \end{aligned} \quad (4)$$

where  $\mathbf{R} = [R_1 \ R_2 \ \cdots \ R_N]^T$  is an  $N \times 1$  column vector, with  $R_n$  representing the total intensity of the reference beam in the  $n$ th measurement,  $\langle R \rangle = \frac{1}{N} \sum_{n=1}^N R_n$  is similar to  $\langle B \rangle$ , and  $\Delta \mathbf{T}$  denotes the differential components of the transmission coefficient.

For GI technology, there are two sources of noise in reconstructed images: noise introduced in the data processing and noise existing in the actual measurement of the object arm and reference arm. By improving the imaging algorithm, the first kind of noise can be suppressed. However,

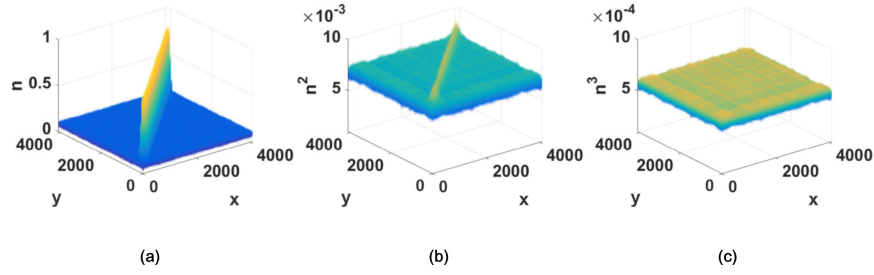


Fig. 2. Comparison of different order terms for the original noise term: (a)  $\mathbf{n}$ , (b)  $\mathbf{n}^2$ , and (c)  $\mathbf{n}^3$ .  $x$  is the row index of the matrices and  $y$  is the column index of the matrices; the speckle patterns are  $128 \times 128$  pixels and the number of measurements,  $N$ , is 3000.

having noise in the practical measurement is inevitable. The data obtained in the experiment can be regarded as the sum of ideal data and noise. A good imaging algorithm should minimize the influence of noise in the optical path.

First, assuming that there is no noise in the experimental environment, we only discuss the noise introduced in the reconstruction process. Obviously,  $\mathbf{A} = \frac{1}{N} \Psi^T \Psi = \mathbf{s} + \mathbf{n}$ , representing the covariance matrix, in Eqs. (3) and (4) directly influences the quality of the imaging. We denote  $\mathbf{s} = \text{diag}(\mathbf{A}) = \text{diag}[D(I_N(1, 1)), D(I_N(1, 2)), \dots, D(I_N(p, q))]$  as the diagonal of  $\mathbf{A}$ , representing the beneficial part in  $\mathbf{A}$ , where  $D(I_N(x, y)) = \frac{1}{N} \sum_{n=1}^N (I_n(x, y) - \langle I_N(x, y) \rangle)^2$  represents the variance of  $I_n(x, y)$ . Then  $\mathbf{n} = \mathbf{A} - \text{diag}(\mathbf{A})$  is the noise term and is given by

$$\mathbf{n} = \begin{bmatrix} 0 & \text{Cov}(I_N(1, 1), I_N(1, 2)) & \dots & \text{Cov}(I_N(1, 1), I_N(p, q)) \\ \text{Cov}(I_N(1, 2), I_N(1, 1)) & \ddots & & \vdots \\ \vdots & & & \text{Cov}(I_N(p, q-1), I_N(p, q)) \\ \text{Cov}(I_N(p, q), I_N(1, 1)) & \dots & \text{Cov}(I_N(p, q), I_N(p, q-1)) & 0 \end{bmatrix} \quad (5)$$

where  $\text{Cov}(I_N(x_1, y_1), I_N(x_2, y_2)) = \frac{1}{N} \sum_{n=1}^N (I_n(x_1, y_1) - \langle I_N(x_1, y_1) \rangle)(I_n(x_2, y_2) - \langle I_N(x_2, y_2) \rangle)$  is the covariance of  $I_n(x_1, y_1)$  and  $I_n(x_2, y_2)$ .

Because all points obey the same distribution, with the increase of the number of measurements, the elements in  $\mathbf{s}$  tend to be consistent with the statistical law, that is, the  $D(I_N(x, y))$ , and then approach the unit matrix  $\mathbf{E}$  after normalization. Therefore, this is only a small part of the noise in the reconstruction process, and the main source of noise comes from the noise term  $\mathbf{n}$ . The elements in  $\mathbf{n}$  show the statistical correlation of any two points in speckles, and these noises accumulate large errors in matrix multiplication. Therefore, reducing the level of the noise term is a valid method to improve imaging quality.

The noise term matrices of the first to third orders are shown in Figs. 2(a)–2(c) and the noise level, which is the average of the noise term matrices, is shown in Fig. 3. The noise term  $\mathbf{n}$  and its high-order terms are all normalized by the maximum value of matrix  $\mathbf{A}$ . As shown in Fig. 2, the distribution of noise terms has no typical noise characteristics. Because the speckle field has speckle size, adjacent pixels are correlated and there is a peak with a certain width near the diagonal. Because the normalized noise is less than 1, the noise values decrease with the increase of order. As shown in Figs. 2 and 3, with the increase of the noise term order, the noise level decreases exponentially and the fluctuation of the noise item also accordingly decreases. The noise gradually becomes similar to a Gaussian distribution that fluctuates in a small range and its average is very small. Hence, it is possible to improve the quality of imaging by reducing the noise level through high-order terms of  $\mathbf{n}$  in theory.

To achieve this, we propose a new method based on the binomial theorem. First, we reintroduce the original reconstruction results back into Eq. (1) several times to acquire high-order terms of  $\mathbf{n}$

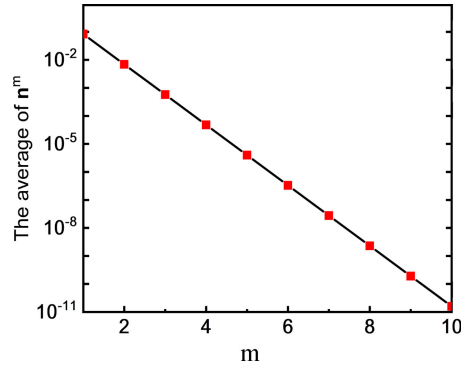


Fig. 3. The noise level  $n^m$  for different orders  $m$ . The speckle patterns are  $128 \times 128$  pixels and the number of measurements,  $N$ , is 3000.

with lower noise, as shown in Figs. 2 and 3:

$$B_n^{(m)} = \sum_{x,y} T_{GI}^{(m-1)}(x,y) I_n(x,y)$$

$$T_{GI}^{(m)}(x,y) = \frac{1}{N} \sum_{n=1}^N \left( B_n^{(m)} - \langle B \rangle^{(m)} \right) \left( I_n(x,y) - \langle I_N(x,y) \rangle \right) \quad (6)$$

where  $T_{GI}^{(m)}(x,y)$  is the imaging results in the  $m$ th correlation calculation and  $B_n^{(m)}$  and  $\langle B \rangle^{(m)}$  represent  $B_n$  and  $\langle B \rangle$  in the  $m$ th calculation. Especially,  $T_{GI}^{(0)}(x,y)$  denotes the object's original transmission coefficient  $T(x,y)$  and  $T_{GI}^{(1)}(x,y)$  denotes the object's original GI result  $T_{GI}(x,y)$ .

Here, assume that matrix  $\mathbf{s}$  is a unit matrix. From Eq. (3), the matrix form of Eq. (6) can be written as follows:

$$\begin{aligned} T_{GI}^{(1)} &= \frac{1}{N} \Psi^T \Psi T = (\mathbf{s} + \mathbf{n}) T \approx (\mathbf{E} + \mathbf{n}) T \\ T_{GI}^{(2)} &= \frac{1}{N} \Psi^T \Psi T_{GI}^{(1)} = (\mathbf{s} + \mathbf{n})^2 T \approx (\mathbf{E} + \mathbf{n})^2 T = (\mathbf{E} + 2\mathbf{n} + \mathbf{n}^2) T \\ &\vdots \\ T_{GI}^{(m)} &= \frac{1}{N} \Psi^T \Psi T_{GI}^{(m-1)} = (\mathbf{s} + \mathbf{n})^m T \approx (\mathbf{E} + \mathbf{n})^m T = \sum_{r=0}^m C_m^r \mathbf{n}^r T \end{aligned} \quad (7)$$

where  $\mathbf{T}_{GI}^{(m)} = [T_{GI}^{(m)}(1,1) \ T_{GI}^{(m)}(1,2) \ \dots \ T_{GI}^{(m)}(p,q)]^T$  is a column vector about  $T_{GI}^{(m)}(x,y)$ . Based on the binomial theorem, we can construct a series of equations with Eqs. (3) and (7) to replace  $\mathbf{n}$  with  $\mathbf{n}^m$  in the reconstruction formula. Because the higher order noise term has lower noise, the reconstruction results with higher order terms will theoretically yield better imaging results.

High-order terms  $\mathbf{n}^m$  can be written as

$$\begin{aligned} \mathbf{n}^m &= [(\mathbf{E} + \mathbf{n}) - \mathbf{E}]^m \\ &= \sum_{r=0}^m C_m^r (-1)^{m-r} (\mathbf{E} + \mathbf{n})^r \end{aligned} \quad (8)$$

and, based on Eq. (8), the higher order term  $n^m$  multiplied by the transmission coefficient  $T$  can make an approximation to take advantage of the previous results from Eq. (7):

$$\begin{aligned}
 n^m T &= [(E + n) - E]^m T \\
 &= \sum_{r=0}^m C_m^r (-1)^{m-r} (E + n)^r T \\
 &= (-1)^m T + \sum_{r=1}^m C_m^r (-1)^{m-r} (E + n)^r T \\
 &\approx (-1)^m T + \sum_{r=1}^m C_m^r (-1)^{m-r} T_{GI}^{(r)}
 \end{aligned} \tag{9}$$

Therefore, when  $m$  is an odd number, then

$$\begin{aligned}
 T_{BGI}^{(m)} &= T + n^m T \\
 &= \sum_{r=1}^m C_m^r (-1)^{m-r} (E + n)^r \\
 &\approx \sum_{r=1}^m C_m^r (-1)^{m-r} T_{GI}^{(r)} \\
 &= \sum_{r=1}^m \lambda_r T_{GI}^{(r)}
 \end{aligned} \tag{10}$$

and, when  $m$  is an even number, then

$$\begin{aligned}
 T_{BGI}^{(m)} &= T - n^m T \\
 &= \sum_{r=1}^m C_m^r (-1)^{m-r+1} (E + n)^r \\
 &\approx \sum_{r=1}^m C_m^r (-1)^{m-r+1} T_{GI}^{(r)} \\
 &= \sum_{r=1}^m \lambda_r T_{GI}^{(r)}
 \end{aligned} \tag{11}$$

In our method, the imaging process can be denoted as the weighted sum of  $T_{GI}^{(r)}$  with Eqs. (10) and (11), where  $\lambda_r$  is the weighting factor and  $T_{BGI}^{(m)}$ , referred to as the  $m$ th-order BGI, is the result when the order of the noise term is  $m$ . Because there is no matrix multiplication and construction in the calculation, our method can be written as an algebraic formula to reduce memory resource consumption without constructing the immense observation matrix  $\Phi$ . In addition, the principles of GI and DGI are similar, as seen in Eqs. (3) and (4), so our method is also effective for DGI. Then our methods can be denoted as

$$T_{BGI}^{(m)} = \sum_{r=1}^m \lambda_r T_{GI}^{(r)} \tag{12}$$

$$T_{BDGI}^{(m)} = \sum_{r=1}^m \lambda_r T_{DGI}^{(r)} \tag{13}$$



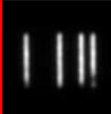
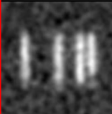

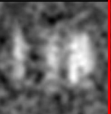
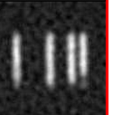

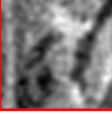

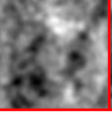

	Original Image	Original DGI	Intermediate Process		Our Method
N=3000, 128*128	$T$	$T_{DGI}^{(1)}$	$T_{DGI}^{(2)}$	$T_{DGI}^{(3)}$	$T_{BDGI}^{(3)}$
<i>Slits</i>					
<i>Lena</i>					

Fig. 4. Comparison of the intermediate process and the final results obtained by using a third-order BDGI for grayscale images “Lena” and binary images “Slits”; the images are both  $128 \times 128$  pixels and the number of measurements,  $N$ , is 3000.

Our method can be written in the unified form of weighted sums, as shown in Eqs. (12) and (13), where the weighting factor is expressed by  $\lambda_r$ .  $\lambda_r$  is the product of positive and negative coefficients and binomial coefficients as shown in Eqs. (10) and (11). For BGI and BDGI with the same order  $m$ , the  $\lambda_r$  factor is the same. For different orders  $m$ , the  $\lambda_r$  factor are different, where  $\lambda_r = C_m^r (-1)^{m-r}$  when  $m$  is an odd number and  $\lambda_r = C_m^r (-1)^{m-r+1}$  when  $m$  is an even number.

In addition, for the noise introduced in the measurement, because the method is linear, it will not interfere with the effective signal. The reconstructed result can be considered as the sum of two parts, the effective signal passing through the system and the external noise passing through the system, so the noise existing in the actual measurement may not greatly amplify the effect of this noise on the reconstructed system. We will prove this later in a numerical experiment.

### 3. Experimental and Simulation Results

To verify the performance of our method, numerous numerical experiments were performed. To evaluate the imaging quality of the reconstruction results, the peak signal-to-noise ratio (PSNR) is introduced as a quantitative measure of the degree of similarity between the imaging result and the original image. It is defined as

$$\text{PSNR} = 10 \times \log_{10} \left[ \frac{(2^p - 1)}{MSE} \right] \quad (14)$$

where  $p = 8$  for a 0–255 grayscale image and  $MSE$  represents the mean square error between the original image and the imaging result. The higher the PSNR value is, the smaller the error is between the obtained image and the original image.

To evaluate the performance of the method, we first conducted numerical experimental demonstrations of our method and several common methods to eliminate the effect of inaccuracy and noise in the experiment on performance evaluation. The data of the object path,  $B_n$ , are obtained directly by summing all pixels of the speckle pattern  $I_n(x, y)$  multiplied by the object's transmission coefficient  $T(x, y)$ .

As shown in Fig. 4, we take a third-order BDGI as an example to present the performance of our method intuitively. In the intermediate process, we can see that the images become increasingly blurred with the increasing number of correlation calculations, and the results by our method become clearer. The background noise of “Slits” is significantly reduced and the contour details of “Lena” become clearer. For “Slits,” the DGI result has a fuzzy edge and a low-contrast background. However, the BDGI result is of much higher fidelity. The increased values of PSNR are 2.217 and



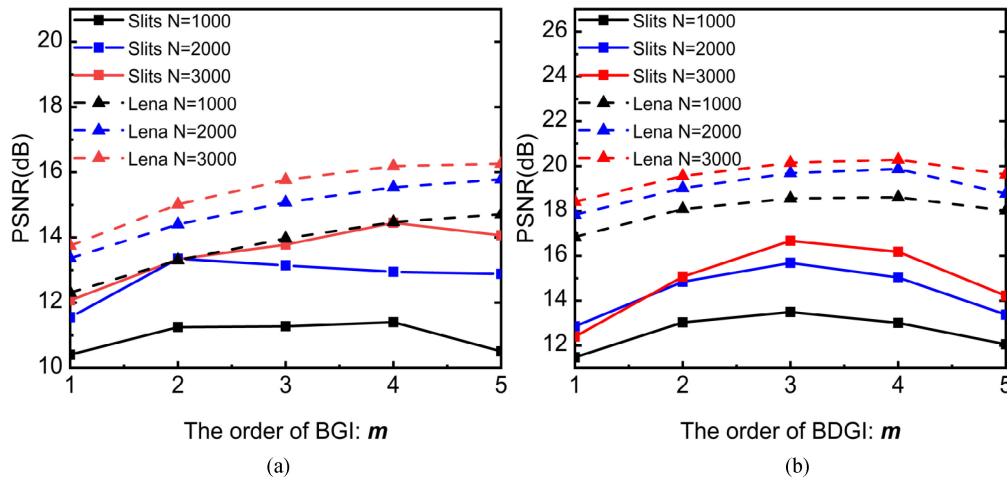


Fig. 5. Relationships between PSNR and the order of (a) BGI and (b) BDGI. The binary images used (“Slits”) and the grayscale images used (“Lena”) are all  $128 \times 128$  pixels and the numbers of measurements,  $N$ , are 1000, 2000, and 3000.

2.6679 dB for the grayscale images “Lena” and the binary images “Slits,” respectively. Although the images with multiple correlation calculations become more and more blurred, more information in the reconstruction process is used by reconstructing  $T_{\text{DGI}}^{(2)}$  and  $T_{\text{DGI}}^{(3)}$ .

According to our principle analysis, as the order increases, the noise level should be reduced to the corresponding order. However, in fact, because of the approximation, it is considered that the effective term  $\mathbf{s}$  is approximately the unit array, where there is a certain amount of error with the strict equality in Eq. (7). In addition, as the number of correlation calculations increases, the more binomial orders are used, and the more error (noise) will be accumulated, which will deteriorate imaging quality. Therefore, we first analyzed the effect of order  $m$  with different numbers of measurements,  $N$ , in Eqs. (12) and (13) on imaging results. The relationship between PSNR and the order of BGI and BDGI with different numbers of measurements is shown in Figs. 5(a) and 5(b), respectively. For each method, experiments for grayscale images “Lena” and binary images “Slits” were conducted. For different orders, the increasing value of PSNR is the same generally with the same change in number of measurements, especially for grayscale images, where the curves are almost parallel. As the number of measurements increases, although the imaging quality of the intermediate process improves, there is little improvement in PSNR. In addition, for the same number of measurements, the PSNRs are not always increasing as the order of the reconstruction formula rises. For BGI, the results are not particularly significant, where the increasing trend is gradually slowing down or decreasing. However, as shown in Fig. 5(b), we can consider that the third-order BDGI offers better PSNR. In addition, owing to the superiority of DGI over GI, the performance of BDGI exceeds that of BGI evidently, especially for grayscale images. Overall, we deem the third-order BDGI to be relatively optimal and thus used this method in the numerical experiments below.

The performance contrast of several methods for binary and grayscale images is demonstrated in Figs. 6(a) and 6(b), and the results when  $N$  is 2000 are shown in Fig. 6(c). In CSGI, the discrete cosine transform (DCT) sparse basis is used to sparse the original signal, and then the orthogonal matching pursuit (OMP) algorithm is used to restore the signal. Finally, the final reconstruction result is obtained by using an inverse DCT transform. For binary images, because of the sparsity of the image, the CSGI results have a great advantage over other methods, as shown in Fig. 6(a) [27], [30], [34]. Therefore, some data points in Fig. 6(a) are omitted, because of its great superiority to other methods. As shown in Fig. 6(c), the CSGI result of “Slits” is very close to the original image, and the PSNR has reached 25.6 dB. Moreover, compared to GI and DGI, the PSNRs of BGI and BDGI are still significantly improved, being 1.93 and 3.05 dB better for 2000 measurements,

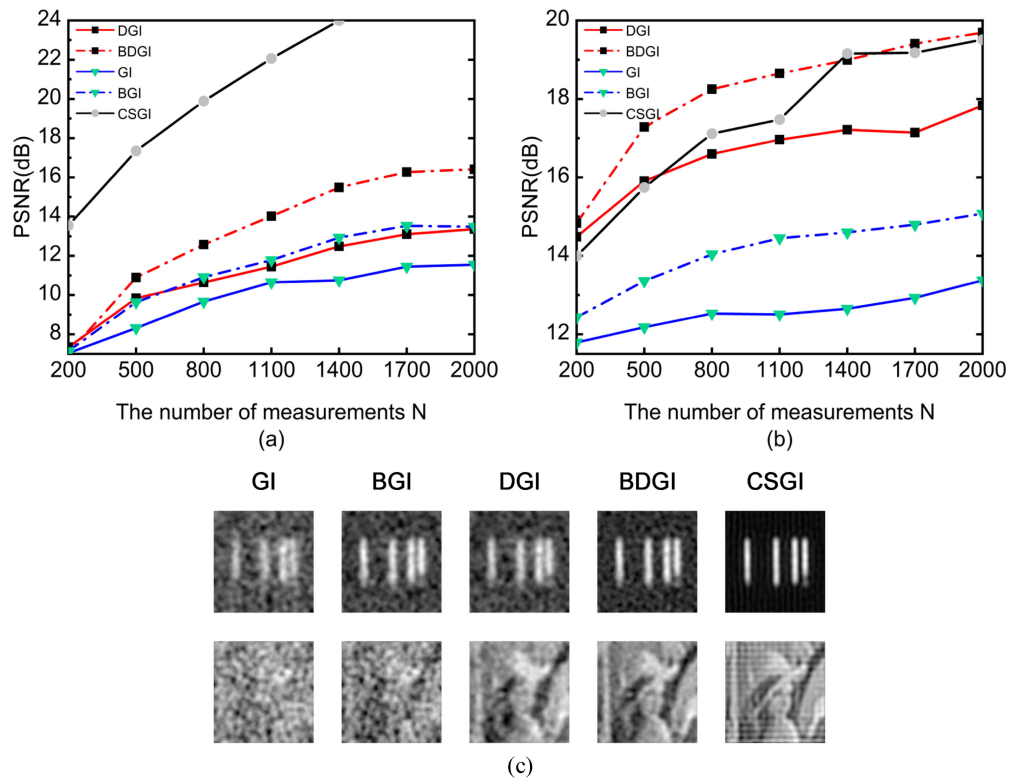


Fig. 6. Relationship between PSNR and the number of measurements,  $N$ , with different reconstruction methods for (a) the binary image "Slits" and (b) the grayscale image "Lena." (c) Comparison of results from different methods with 2000 measurements; the images are  $128 \times 128$  pixels.

respectively. However, for the grayscale image, CSGI offers no superiority and is even worse than BDGI when the number of measurements is small. The PSNR values of BDGI and CSGI are 1.7 dB higher than that of BGI for 2000 measurements. In Fig. 6(c), both BDGI and CSGI achieve generally satisfactory reconstruction performance, although the visual effects of CSGI are better than those of BDGI. Therefore, BDGI can enhance imaging quality to a generally satisfactory level on the basis of DGI.

Robustness is an important indicator for imaging systems. Anti-interference performance is a major factor in evaluating whether a system can be applied in practice, because noise in the optical path is inevitable. To verify anti-interference performance, MATLAB numerical experiments were conducted. The experimental results of "Slits" and "Lena" against noise, shown in Figs. 7(a) and 7(b), show the properties of binary images and grayscale images, respectively. Additive white Gaussian noise (AWGN) was added to the object path, that is, the vector  $\mathbf{B}$ . As the curves indicate in both Figs. 7(a) and 7(b), BDGI exhibits better performance against AWGN than does CSGI. High SNR of  $\mathbf{B}$  is needed for CSGI as shown in Fig. 7(a), where the curve drops steeply from 70 dB, whereas the value for BDGI is 30 dB. Similarly, the values where the curves begin to drop are 50 and 60 dB for BDGI and CSGI, respectively, in Fig. 7(b). Above, BDGI has a better tolerance for noise than CSGI. Furthermore, the PSNRs for CSGI and BDGI are similar ( $\sim 19.5$  dB) for "Lena" with high SNR. By using a compressed sensing algorithm, CSGI only has advantages for binary images that have high sparsity. Therefore, BDGI has better robustness to AWGN than CSGI, being closer to DGI, and BDGI can obtain high imaging quality similar to that of CSGI for grayscale images.

Another reason limiting practical application of the GI technique is its long computing time. The calculation time of several methods compared to the number of measurements is shown in Fig. 8. Time is measured starting from reading the image from the hard disk. Because of the same

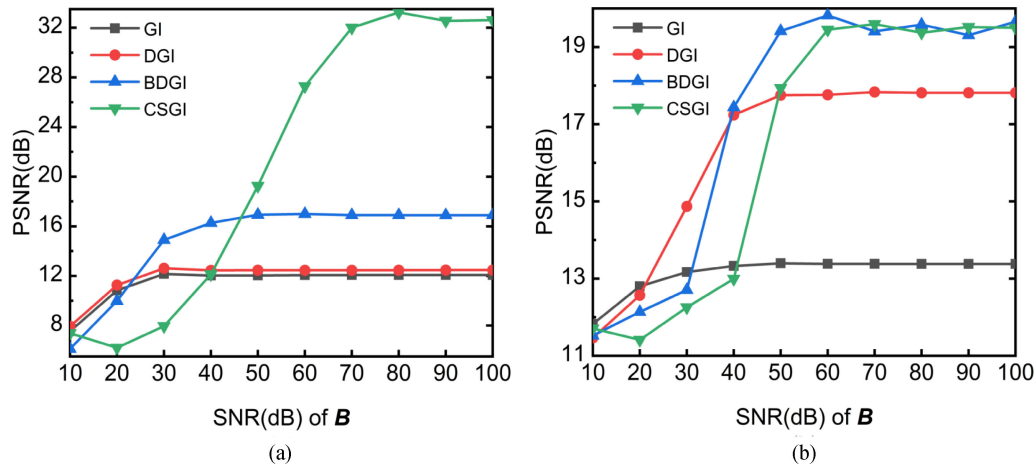


Fig. 7. Relationship between PSNR and the SNR (dB) of the object path's total light intensity  $B$ . The images are (a) the binary image "Slits" and (b) the grayscale image "Lena," both of  $128 \times 128$  pixels, respectively, and the numbers of measurements are all 3000.

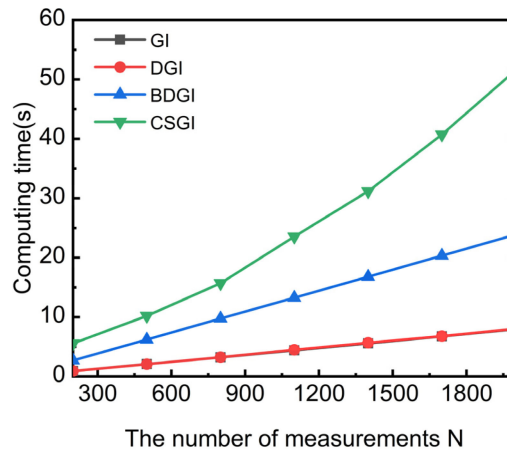


Fig. 8. Relationship between computing time and the number of measurements,  $N$ , by GI, DGI, BDGI, and CSGI. The image used was "Lena" and speckles are  $128 \times 128$  pixels. (Computer configuration: Intel Xeon CPU E5-1650V4, 3.6 GHz; RAM: 64.0 GB.).

computational complexity, the two curves for GI and DGI in Fig. 8 coincide. Three DGI operations are performed in the third-order BDGI process, so the computing time is a factor of 3 higher than that of GI (DGI). In addition, CSGI costs more and more time with the number of measurements increasing, whereas computing time for BDGI increases just linearly. Owing to the compressed sensing algorithm, CSGI requires the construction of a large observation matrix ( $N \times K$ ), where the large number of measurements,  $N$ , and the giant image with numerous pixels,  $K$ , will lead to long computing time. Furthermore, for grayscale images, BDGI yields a similar imaging effect to that of CSGI as shown in Fig. 6, so it may be advantageous. Accordingly, less time is spent in BDGI than in CSGI, especially for a large number of measurements or a large image with many pixels. Moreover, only an algebraic formula is used in our method, so fewer memory resources are used without the need to construct and compute a huge matrix.

To prove the validity with noise and error of this method in practice, experimental results of "Slits" ( $100 \times 100$  pixels) reconstructed by various methods with different numbers of measurements,  $N$ , are shown in Figs. 9 and 10. The experimental system was set up as shown in Fig. 1, where

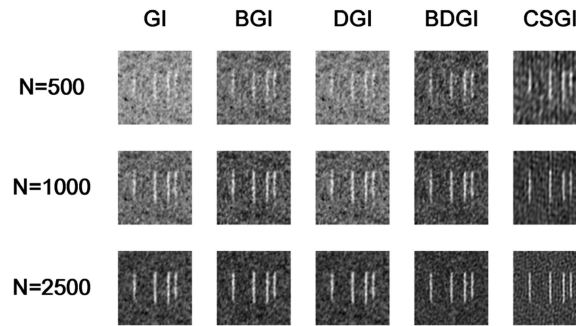


Fig. 9. Experimental results of  $100 \times 100$  pixel image “Slits” obtained by GI, BGI, DGI, BDGI, and CSGI for 500, 1000, and 2500 measurements. The orders of BGI and BDGI are both 3.

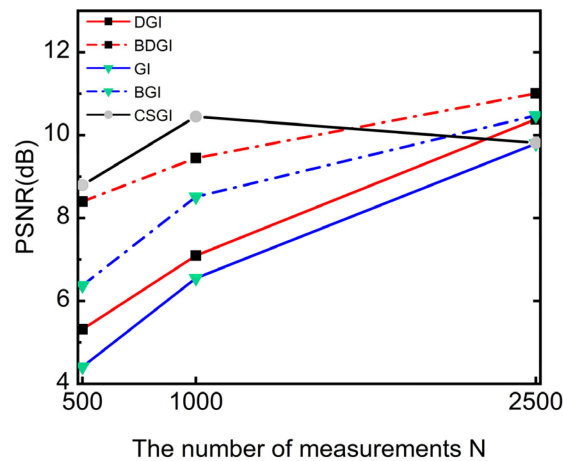


Fig. 10. Experimental results between PSNR and the number of measurements,  $N$ , of  $100 \times 100$  pixel image “Slits” obtained by GI, BGI, DGI, BDGI, and CSGI. The orders of BGI and BDGI are both 3.

$Z_1 = Z_2 = 650$  mm, the focal length  $f$  of the lens was 250 mm, and the transmission aperture of the lens was  $L_1 = 10$  mm. The object was the same as the previous binary image: “Slits” (slit width  $a = 30 \mu\text{m}$ , slit height  $h = 300 \mu\text{m}$ , and center-to-center separation  $d = 60, 120, 180 \mu\text{m}$ ). For different methods using the same optical setup, data processing of the image was different, with third-order BGI and BDGI being used.

The results in Figs. 9 and 10 verify the effectiveness of our method. As the number of measurements,  $N$ , increases, the images become clearer for all the methods. The imaging results reconstructed by using the original GI are contaminated by noise generated in the imaging process. DGI and the third-order BGI can relatively improve the results to some extent. But, the edge is still fuzzy. However, the third-order BDGI continues to enhance the visual effects and reduce the noise level while making the edge of the image distinct. In addition, the great superiority of CSGI in Fig. 6, in which the imaging results are close to the original image, is not reflected. For PSNR, there is no significant difference between BDGI and CSGI. This illustrates that BDGI can achieve performance similar to that of CSGI in actual applications with noise and interference.

#### 4. Conclusion

In conclusion, we have proposed a novel reconstruction approach for GI, BGI, and BDGI. In the new method, the binomial theorem is used to construct weighted sums to reduce the influence of noise introduced by the imaging formula on imaging. Experimental and simulation results show that the

third-order BDGI can enhance the PSNR compared with DGI to achieve satisfactory results. The results have proved that the third-order BDGI can be considered optimal. For grayscale images, the BDGI method can yield similar imaging results to those of CSGI. In addition, it is superior to CSGI in terms of robustness. Above all, CSGI and PGI use the observation matrix to find the least-squares solution of the matrix equation, so their computational complexity and computation time are much higher than those of BDGI. We believe that this technology can further speed up the application process of GI.

## References

- [1] T. B. Pittman, Y. H. Shih, D. V. Strekalov, and A. V. Sergienko, "Optical imaging by means of two-photon quantum entanglement," *Phys. Rev. A*, vol. 52, no. 5, pp. R3429–R3432, 1995.
- [2] D. V. Strekalov, A. V. Sergienko, D. N. Klyshko, and Y. H. Shih, "Observation of two-photon "ghost" interference and diffraction," *Phys. Rev. Lett.*, vol. 74, no. 18, pp. 3600–3603, 1995.
- [3] R. S. Bennink, S. J. Bentley, and R. W. Boyd, "Two-Photon" coincidence imaging with a classical source," *Phys. Rev. Lett.*, vol. 89, no. 11, 2002, Art. no. 113601.
- [4] R. S. Bennink, S. J. Bentley, R. W. Boyd, and J. C. Howell, "Quantum and classical coincidence imaging," *Phys. Rev. Lett.*, vol. 92, no. 3, 2004, Art. no. 033601.
- [5] A. Gatti, E. Brambilla, M. Bache, and L. A. Lugiato, "Ghost imaging with thermal light: Comparing entanglement and classical correlation," *Phys. Rev. Lett.*, vol. 93, no. 9, 2004, Art. no. 093602.
- [6] M. D'Angelo and Y. H. Shih, "Quantum imaging," *Laser Phys. Lett.*, vol. 2, no. 12, pp. 567–596, 2005.
- [7] F. Ferri, D. Magatti, A. Gatti, M. Bache, E. Brambilla, and L. A. Lugiato, "High-resolution ghost image and ghost diffraction experiments with thermal light," *Phys. Rev. Lett.*, vol. 94, no. 18, 2005, Art. no. 183602.
- [8] R. E. Meyers and K. S. Deacon, "Quantum ghost imaging experiments at ARL," *Proc. SPIE*, vol. 7815, no. 2, 2010, Art. no. 781501.
- [9] J. H. Shapiro and R. W. Boyd, "The physics of ghost imaging," *Quantum Inf. Process.*, vol. 11, no. 4, pp. 949–993, 2012.
- [10] S. Q. Nan *et al.*, "Experimental investigation of ghost imaging of reflective objects with different surface roughness," *Photon. Res.*, vol. 5, no. 4, pp. 372–376, 2017.
- [11] P. Ryczkowski, M. Barbier, A. T. Friberg, J. M. Dudley, and G. Genty, "Ghost imaging in the time domain," *Nat. Photon.*, vol. 10, no. 3, pp. 167–170, 2016.
- [12] B. I. Erkmen and J. H. Shapiro, "Ghost imaging: From quantum to classical to computational," *Adv. Opt. Photon.*, vol. 2, no. 4, pp. 405–450, 2010.
- [13] P. A. Moreau, E. Toninelli, T. Gregory, and M. J. Padgett, "Ghost imaging using optical correlations," *Laser Photon. Rev.*, vol. 12, no. 1, 2017, Art. no. 1700143.
- [14] M. J. Padgett and R. W. Boyd, "An introduction to ghost imaging: Quantum and classical," *Philos. Trans. Roy. Soc. A*, vol. 375, no. 2099, 2017, Art. no. 20160233.
- [15] D. Zhang, Y. H. Zhai, L. A. Wu, and X. H. Chen, "Correlated two-photon imaging with true thermal light," *Opt. Lett.*, vol. 30, no. 18, pp. 2354–2356, 2005.
- [16] N. A. Tian, Q. C. Guo, A. L. Wang, D. L. Xu, and L. Fu, "Fluorescence ghost imaging with pseudothermal light," *Opt. Lett.*, vol. 36, no. 16, pp. 3302–3304, 2011.
- [17] S. Karmakar, R. Meyers, and Y. Shih, "Ghost imaging experiment with sunlight compared to laboratory experiment with thermal light," *Proc. SPIE*, vol. 8518, no. 2, 2012, Art. no. 851805.
- [18] H. Wu, C. L. Wang, and W. L. Gong, "Ghost imaging via sparse structured illumination source," *Opt. Exp.*, vol. 26, no. 4, pp. 4183–4191, 2018.
- [19] D. Pelliccia, A. Rack, M. Scheel, V. Cantelli, and D. M. Paganin, "Experimental x-ray ghost imaging," *Phys. Rev. Lett.*, vol. 117, no. 21, 2016, Art. no. 113902.
- [20] X. P. Wang and Z. H. Lin, "Nonrandom microwave ghost imaging," *IEEE Trans. Geosci. Remote*, vol. 56, no. 8, pp. 4747–4764, Aug. 2018.
- [21] P. L. Zhang, W. L. Gong, X. Shen, and S. S. Han, "Correlated imaging through atmospheric turbulence," *Phys. Rev. A*, vol. 82, no. 3, 2010, Art. no. 033817.
- [22] W. L. Gong and S. H. Han, "Correlated imaging in scattering media," *Opt. Lett.*, vol. 36, no. 3, pp. 394–396, 2011.
- [23] X. Yao, W. Zhang, H. Li, L. X. You, Z. Wang, and Y. D. Huang, "Long-distance thermal temporal ghost imaging over optical fibers," *Opt. Lett.*, vol. 43, no. 4, pp. 759–762, 2018.
- [24] C. J. Deng, L. Pan, C. L. Wang, X. Gao, W. L. Gong, and S. S. Han, "Performance analysis of ghost imaging lidar in background light environment," *Photon. Res.*, vol. 5, no. 5, pp. 431–435, 2017.
- [25] B. I. Erkmen, "Computational ghost imaging for remote sensing," *J. Opt. Soc. Amer. A*, vol. 29, no. 5, pp. 782–789, 2012.
- [26] P. Clemente, V. Duran, V. Torres-Company, E. Tajahuerce, and J. Lancis, "Optical encryption based on computational ghost imaging," *Opt. Lett.*, vol. 35, no. 14, pp. 2391–2393, 2017.
- [27] O. Katz, Y. Bromberg, and Y. Silberberg, "Compressive ghost imaging," *Appl. Phys. Lett.*, vol. 95, no. 13, 2009, Art. no. 131110.
- [28] F. Ferri, D. Magatti, L. A. Lugiato, and A. Gatti, "Differential ghost imaging," *Phys. Rev. Lett.*, vol. 104, no. 25, 2010, Art. no. 219902.
- [29] W. L. Gong and S. S. Han, "A method to improve the visibility of ghost images obtained by thermal light," *Phys. Lett. A*, vol. 374, no. 8, pp. 1005–1008, 2010.

- [30] P. Zerom, K. W. C. Chan, J. C. Howell, and R. W. Boyd, "Entangled-photon compressive ghost imaging," *Phys. Rev. A*, vol. 84, no. 6, 2011, Art. no. 061804.
- [31] B. Q. Sun, S. S. Welsh, M. P. Edgar, J. H. Shapiro, and M. J. Padgett, "Normalized ghost imaging," *Opt. Exp.*, vol. 20, no. 15, pp. 16892–16901, 2012.
- [32] W. Wang, Y. P. Wang, J. H. Li, X. X. Yang, and Y. Wu, "Iterative ghost imaging," *Opt. Lett.*, vol. 39, no. 17, pp. 5150–5153, 2014.
- [33] X. R. Yao *et al.*, "Iterative denoising of ghost imaging," *Opt. Exp.*, vol. 22, no. 20, pp. 24268–24275, 2014.
- [34] C. Zhang, S. X. Guo, J. S. Cao, J. Guan, and F. L. Gao, "Object reconstitution using pseudo-inverse for ghost imaging," *Opt. Exp.*, vol. 22, no. 24, pp. 30063–30073, 2014.
- [35] W. L. Gong, "High-resolution pseudo-inverse ghost imaging," *Photon. Res.*, vol. 3, no. 5, pp. 234–237, 2015.
- [36] M. J. Sun, M. F. Li, and L. A. Wu, "Nonlocal imaging of a reflective object using positive and negative correlations," *Appl. Opt.*, vol. 54, no. 25, pp. 7494–7499, 2015.
- [37] C. Yang *et al.*, "Scalar-matrix-structured ghost imaging," *Photon. Res.*, vol. 4, no. 6, pp. 281–285, 2016.
- [38] H. W. Zhang, S. X. Guo, C. Zhang, C. Yang, J. S. Cao, and F. L. Gao, "Pseudo-inverse iterative denoising method for object reconstruction of ghost imaging," *Acta Photon. Sin.*, vol. 46, no. 2, 2017, Art. no. 210001.
- [39] X. F. Lv *et al.*, "Experimental investigation of iterative pseudoinverse ghost imaging," *IEEE Photon. J.*, vol. 10, no. 3, Jun. 2018, Art. no. 3900708.
- [40] L. Wang and S. Zhao, "Fast reconstructed and high-quality ghost imaging with fast walsh–hadamard transform," *Photon. Res.*, vol. 4, no. 6, pp. 240–244, 2016.
- [41] D. W. Liu *et al.*, "Complementary normalized compressive ghost imaging with entangled photons," *IEEE Photon. J.*, vol. 10, no. 2, Apr. 2018, Art. no. 7500507.